3
Electronic Structure of Molecular Solids: Bridge to the Electrical Conduction

Nobuo Ueno

3.1
Introduction

Organic semiconductors, discovered in the mid-twentieth century [1–3], have larger bandgap and smaller bandwidth than their inorganic counterparts. The number of thermally excited carriers in the organic films is not enough to give sufficient current. We thus need injection of carriers into the organic film from electrodes to realize sufficient current in organic devices. This chapter describes fundamental aspects of electronic structure of organic semiconductors and the method to bridge the electronic structure and electrical property using ultraviolet photoemission spectroscopy (UPS).

As it is well known, the electrical conductivity (σ) is given by

$$\sigma = nq\mu \tag{3.1}$$

where n is the carrier concentration, q is the charge of the carrier concerned, and μ is the charge-carrier mobility. This relation simply indicates that we must increase n and μ, if we need larger conductivity and electrical current. To obtain sufficient current in organic films, we need to inject charge carriers effectively from electrodes to increase n. As the carrier injection is dominated by the charge injection barrier height that is the energy difference between the Fermi level (E_F) and the highest occupied molecular orbital (HOMO) state (for hole) or the lowest unoccupied molecular orbital (LUMO) state (for electron) of the organic film, a large number of studies using UPS have been carried out to study the energy level alignment at organic/metal interfaces [4–9]. These experiments have provided quantitative information on the position of E_F in the HOMO–LUMO bandgap of an organic layer at organic/metal or organic/organic heterojunctions and motivated studies on the origin of the Fermi level pinning to give models such as the charge neutrality level and/or the induced density of interface states [10–18] and the integer charge transfer states (ICT model) due to polaron [19–21] in the bandgap at the interfaces. Unfortunately, however, direct experimental evidence of such bandgap

Physics of Organic Semiconductors, Second Edition. Edited by Wolfgang Brütting and Chihaya Adachi

states has been missing for weakly interacting interfaces that show pinning of the Fermi level near HOMO or LUMO. In relation to this Fermi level pinning effect, we observe n-or p-type charge transport property without intentional impurity doping. These effects seem to be determined by the host molecule itself. There have also been some direct measurements on gap states that have not been detected by conventional UPS, which have pointed out the role of the gap states in the energy level alignment and band bending phenomena [22–26].

To increase μ, on the other hand, we need to know principal origin of μ of organic material concerned, namely, coherent band conduction or hopping conduction. The band mobility, which is derived by coherent carrier motion and generally larger than the hopping mobility, is dominated by the energy band dispersion [27, 28], whereas the hopping mobility is dominated by the charge reorganization energy that is related to electron or hole/vibration coupling [28–32]. Unfortunately, however, quantum mechanical/chemical information on the charge mobility has been completely left to be elusive in experimental field till 2002 due to difficulty in realizing high-energy resolution UPS measurements on organic thin films [33, 34]. Such fundamental understanding based on experimental evidences is critical if we are going to improve charge-carrier mobility from quantum chemical molecular design and material engineering.

In this way, electronic structure of the organic semiconductor is of critical importance to unravel electrical conduction in organic devices [28]. Many of the electrical properties of organic devices have not been discussed based on quantum mechanical or quantum chemical ways, but on classical electromagnetism. In this chapter, we describe a feature of electronic states of an organic molecular solid in relation to the charge transport property.

3.2
General View of Electronic States of Organic Solids

3.2.1
From Single Molecule to Molecular Solid

We will first learn the evolution of electronic structure from single molecule to molecular solid and then discuss the energy bands typically appearing in the solid. Figure 3.1a schematically shows the electronic structure of a polyatomic molecule, where the molecule is made of three atoms. The ordinate is the electron energy. The potential well is formed by the Coulombic potential of each atomic nucleus. The effective potential well of the molecule for an electron is formed by the atomic nuclei as well as other electrons. However, we here neglect contribution of other electrons for simplicity. The wells of the nuclei are merged in the upper part to form a broad well, where various molecular orbitals (MOs) exist and produce discrete energy levels that are different from atomic energy levels. Each MO level (energy level) is occupied by two electrons with spin up and down, respectively. The horizontal part of the potential well is the vacuum level (VL), at which an electron that exists outside the

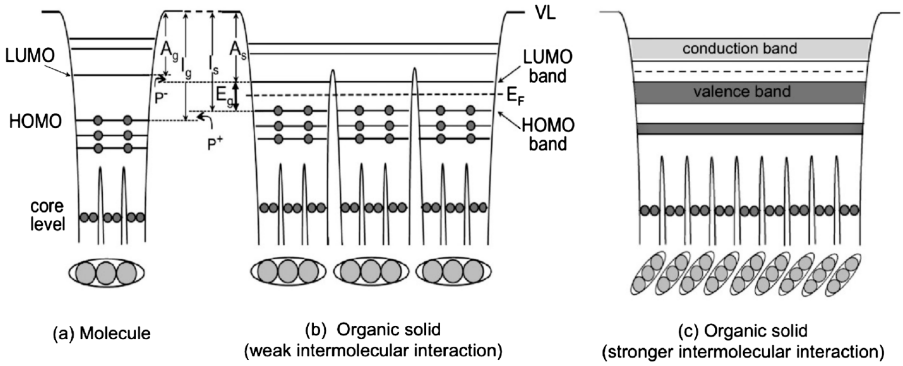

Figure 3.1 Evolution of electronic structure, from single molecule (a) to solid (b and c). When intermolecular electronic interaction is weak, the width of energy bands is very narrow (b). With increase in the intermolecular interaction, the bandwidth becomes larger (c). VL: the vacuum level, E_F: Fermi level, A_g: electron affinity of gas phase, A_s: electron affinity of solid, I_g: ionization energy of gas phase, I_s: ionization energy of solid, P^-: polarization energy for negative ion in solid, P^+: polarization energy for positive ion in solid, E_g: bandgap.

molecule stops moving and its kinetic energy is zero. The electron excited above the VL can escape from the molecule to vacuum. Electrons at deeper levels are localized in the atomic potential well (core levels), and thus have the feature of those in atomic orbitals because of very high potential barrier between the atoms. The upper energy levels, MO levels, involve interatomic interaction to form delocalized molecular orbitals. The energy separations from the HOMO or the LUMO to the VL are defined as the gas-phase ionization energy (I_g) or the electron affinity (A_g) of the molecule, respectively. When molecules come together to form an organic solid, the electronic structure becomes like that shown in Figure 3.2b. Since the molecules interact only by the weak van der Waals interaction in many organic solids, wave functions of the occupied valence states (or valence bands) and the lower unoccupied states (conduction bands) are mainly localized in each molecule, yielding narrow intermolecular energy band of the bandwidth approximately <0.2 eV [28]. Thus, the electronic structure of an organic solid approximately preserves that of a molecule, and the validity of usual band theory is often limited in discussing charge transport in an organic solid [28], which means that such an organic solid often shows two faces, in some cases face of single molecule and in other cases face of solid state. This situation in the electronic structure of the solid allows us to simply write the band structure such as the HOMO and the LUMO levels by using "line" due to very narrow bandwidth as in Figure 3.1b. When intermolecular interaction becomes larger, both the occupied (valence) and unoccupied (conduction) bands become wider because of larger overlapping of relevant wave functions (MOs) of adjacent molecules. This also means that the HOMO does not necessarily show the widest band in occupied valence bands, since the bandwidth is related to spatial spread of the MO as well as the intermolecular distance. Such an example can be seen in the intermolecular band dispersion results on perylene-3,4,9,10-tetracarboxilic dianhydride (PTCDA) [35].

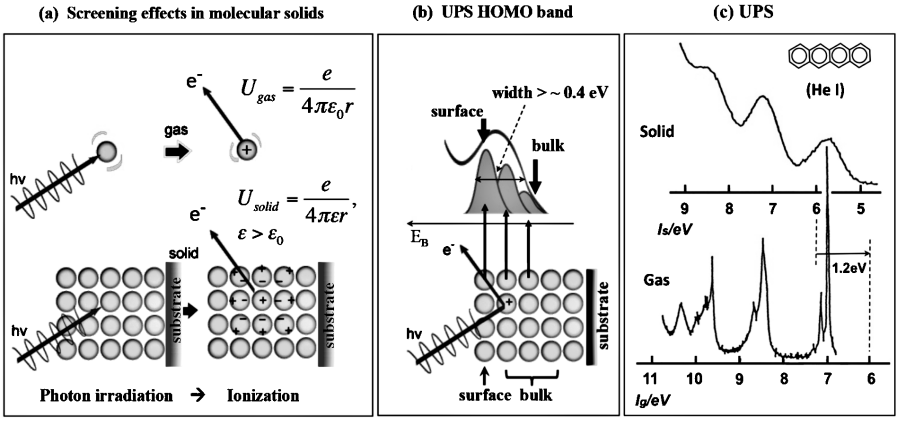

Figure 3.2 Screening effects in an organic semiconductor film and in a gas-phase molecule (a) and origin of the bandwidth of a UPS feature for a thin film of weakly interacting molecules (b). The potential (U) of the photogenerated hole (positive ion) acting on the photoelectron is described in (a). Panel (b) illustrates a historical model that UPS bandwidth is determined by superposition of photoelectrons from surface molecules (with low kinetic energy/higher binding energy) and bulk molecules (with higher kinetic energy/lower binding energy), where screening effects depend on the number of molecules surrounding the ion. Panel (c) show comparison of gas and thin-film UPS on naphthacene, where the ionization energy of gas-phase spectrum is shifted by ~1.2 eV, polarization energy (P^+), to align the HOMO positions.

From a molecule to a solid, the energy levels change from Figure 3.1a to b, where I_g and A_g become the ionization energy (I_s) and the electron affinity (A_s) of the solid, respectively. They are defined as the energy separation of the HOMO and the LUMO from the VL, as in the case of a molecule (Figure 3.1b). When a hole (electron) is introduced into the HOMO (LUMO) of the solid, the electronic polarization of the molecules surrounding the ionized molecule stabilizes the ion by screening effects, leading to a lowering of I and an increase in A from those in the gas phase, as shown in Figure 3.1a and b. As the polarization effect may be different for the hole (cation) and the electron (anion) because a molecular solid is not complete continuum medium, there are two polarization energies P^+ and P^- for the hole and the electron, respectively [36, 37]; thus, we write

$$I_s = I_g - P^+, \quad A_s = A_g + P^- \tag{3.2}$$

This relation is easily understandable by considering the case of photoionization of a molecule and a molecular solid. The potential energy of an electron in the attractive force field of the ion is $U = e^2/4\pi\varepsilon_0 r$ in vacuum, where ε_0 is the vacuum permittivity, and $U = e^2/4\pi\varepsilon r$ in the solid with the permittivity ε that reflects screening of the ion by surrounding molecules, where the molecules are polarized as shown in Figure 3.2. UPS of organic thin films gives I_s that is smaller by P^+ than I_g, and inverse photoemission spectroscopy (IPES) provides A_s larger by P^- than A_g.

Although we usually do not write a hole in the occupied MO level but two electrons in the energy level scheme, the scheme always means that the occupied MO

level corresponds to that of one hole state and the unoccupied MO level to one electron state by assuming Koopmans' theorem [38, 39]. For ionization, Koopmans' theorem gives

$$E_N - E_{N-1} = \varepsilon_i \tag{3.3}$$

where E_N and E_{N-1} are total electron energies of N and $N-1$ electron systems in closed-shell Hartree–Fock approximation, respectively, and ε_i is the orbital energy of ith level from which an electron is ejected. Therefore, the computed MO energy corresponds to its ionization energy. The valence band is thus called as hole band and the conduction band as electron band. This is why we can use the energy level diagram in Figure 3.1 for UPS and IPES, and also for hole and electron conduction in organic solid.

3.2.2
Polaron and Charge Transport

In the UPS experiment, as the ionization time can be defined by the time from the photoexcitation to the photoelectron detection, the polarization that is faster than the ionization time contributes to the P^+. This is generally contribution of very rapid electron rearrangement after photoionization. If we consider slower ionization process such as charge hopping (with low mobility), polarization associated with deformation of geometrical structure of the molecular ion (change in the atomic positions within the ion that is related to local phonon/molecular vibration) and of surrounding molecules (crystal phonon) contributes to P^+. In this way, there are three polarization contributions: (i) electronic polarization (fast, and called electronic polaron from quasi-particle picture), (ii) intramolecular geometrical polarization (slower than (i) and here we call as very small polaron,) and (iii) intermolecular geometrical polarization (small polaron if the geometrical deformation is in the scale of the unit cell of the crystal, and large polaron for a larger scale deformation, expected to be slower than (ii)). Thus, P^+ in UPS may mainly involve electronic polarization effects (i), and contribution of (ii) and (iii) has been considered to be too slow to be detected effectively by conventional UPS. Accordingly, UPS measures mainly a positive electronic polaron, while the hopping mobility in devices also involves effects of the very small, small, and large polarons (positive/negative polaron for hole/electron) depending on timescale of the hopping as well as the electronic polaron. Therefore, information on these polarons, especially on polaron binding energy (E_{Pol}: stabilization energy by polarization) and the timescale, is important in discussion of photoionization and charge transport.

3.2.3
Requirement from Thermodynamic Equilibrium

There is key concept for considering electronic state of solid and the energy level alignment at the interface of interacting two solids. The electron system of solid is

specified by the Fermi–Dirac distribution with the Fermi level (E_F). E_F is the chemical potential of the electron (fermion) system. If an organic solid is free from impurity and effective masses (m^*) of the HOMO hole and the LUMO electrons are the same, E_F locates at the center of the HOMO–LUMO gap. Since the electrons fill the energy levels strictly following the Fermi–Dirac distribution, an interface system consisting of two solids must have single E_F throughout the interacting solids when the electrons in this system are in thermodynamic equilibrium after exchange through the interface. This concept should be strictly valid for the electron system in thermodynamic equilibrium.

The work function ϕ of the solid is defined as the energy separation between the E_F and the VL.

3.3 Electronic Structure in Relation to Charge Transport

3.3.1 Ultraviolet Photoemission Spectroscopy

Photoemission spectroscopy, particularly ultraviolet photoemission spectroscopy, is a well-established and the most widely used technique in characterizing valence electronic structure at interfaces, including metal–molecule interfaces and solids (thin films of high resistivity). A schematic UPS process is shown in Figure 3.3, where the energy and momentum conservation rules are used in analyzing observed spectra. As the photogenerated hole exists during the photoionization of a molecular solid, the spectrum reflects the one hole state. Thus, for example, the binding energy (E_B) from E_F can be obtained by the energy conservation rule as

$$E_B = h\nu - E_k - \phi \tag{3.4}$$

where E_k and ϕ are the kinetic energy of photoelectron and the work function of molecular film, respectively. The vacuum level (E_{vac}), at which $E_k = 0$, is identified by the cutoff position of the secondary electron. E_F is measured by UPS of the conductive/metal substrate. In some cases, the binding energy (E_B^v) is measured from E_{vac} as

$$E_B^v = E_B + \phi = h\nu - E_k \tag{3.5}$$

Elimination of the photogenerated hole by electron transfer from the substrate contributes to the broadening of the observed spectral width, if the attractive Coulombic potential acting on the photoelectron disappears by the elimination of the hole before detection of the photoelectron.

In order to obtain the energy band dispersion from UPS experiments, a three-step model is generally adopted for the photoemission process, consisting of an optical dipole excitation in the bulk, followed by transport to the surface and emission to the vacuum [40, 41]. General assumptions are (i) both the energy and the momentum of the electrons are conserved during the optical transition, (ii) the

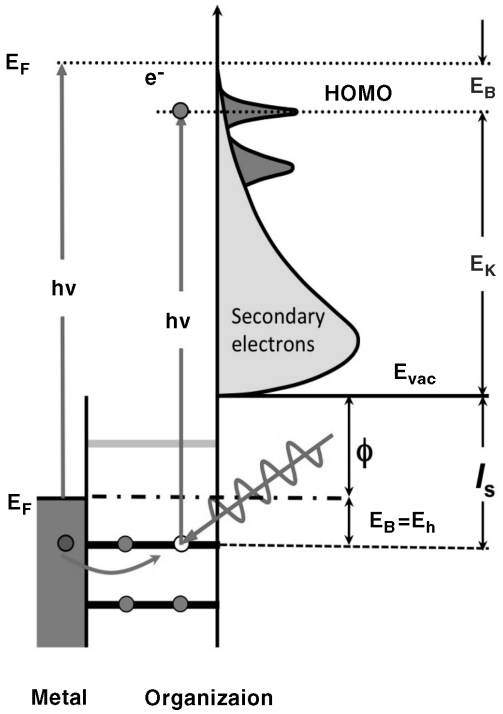

Figure 3.3 Electronic structure probed by ultraviolet photoemission spectroscopy (UPS) and important parameters in discussing organic devices. Here, binding energy (E_B) refers to the Fermi level (E_F). E_k, ϕ, and E_h are the kinetic energy of the photoelectron, work function, and hole injection barrier, respectively.

momentum component parallel to the surface is conserved, while the electron escapes through the surface, and (iii) the final continuum state in the solid is a parabolic free electron-like band in a constant inner potential V_0 :,

$$E = \frac{\hbar^2 \mathbf{k}^2}{2m^*} + V_0 \tag{3.6}$$

where m^* is the effective mass of the photoexcited electron in the final state (conduction band) and $\boldsymbol{k}$ is the electron wave vector (Figure 3.4). V_0 represents the effective potential step to be crossed by the photoexcited electron to leave the surface. The kinetic energy E_{kin} and the wave vector $\boldsymbol{K}$ of observed photoelectron is described by the following relation, with the surface normal ($K^{\perp}$) and parallel ($K^{//}$) components of $\boldsymbol{K}$, respectively,

$$E_{\text{kin}} = \frac{\hbar^2 K^2}{2m_0} = \frac{\hbar^2 \left(K^{\perp^2} + K^{//^2} \right)}{2m_0} \tag{3.7}$$

$$K^{\perp} = K\cos\theta, \quad K^{//} = K\sin\theta \tag{3.8}$$

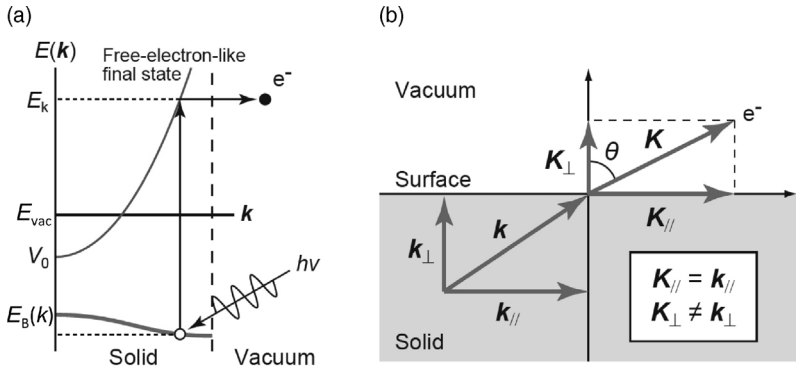

Figure 3.4 Energy and momentum conservation rules for measurements of valence band dispersion $E_B(k)$ (a) and the momentum conservation upon photoelectron escape to vacuum (b).

where m_0 is the free electron mass and θ is the photoelectron emission angle from surface normal (Figure 3.4b). The surface normal and parallel components of the wave vector $\boldsymbol{k}$ of the photoexcited electron in the solid, respectively, can be expressed as

$$k_{\perp} = \sqrt{\frac{2m^*}{\hbar^2}}\sqrt{E_{\mathrm{kin}}\cos^2\theta + V_0} \tag{3.9}$$

$$k_{//} = \sqrt{\frac{2m_0}{\hbar^2}}\sqrt{E_{\mathrm{kin}}}\sin\theta = 0.51A^{-1}\sqrt{E_{\mathrm{kin}}(eV)}\sin\theta \tag{3.10}$$

The binding energy (E_B^v) from E_{vac} of the electron in the initial state is written as Eq. (3.5). The free electron mass m_0 is often assumed for m^* in the computation of $k_{\perp}$. The band dispersion along either $k_{//}$ or $k_{\perp}$ in the organic film may be investigated by changing the electron emission angle θ or E_{kin} of the photoelectrons via tuning of the energy of the incident photons $h\nu$. As understood from Eqs. (3.9) and (3.10), however, the inner potential V_0 must be determined in obtaining $k_{\perp}$, while $k_{//}$ can be determined without V_0. Thus, the simplest way to obtain band dispersion is to measure angle-resolved UPS (ARUPS) of a single-crystal specimen as a function of θ in order to tune $k_{//}$ (method I). A principal difficulty in measuring $k_{//}$ for organic semiconductors and insulators is that electrical conductivity is very low and thus charging of the specimen upon photoemission has hindered to use single-crystal organic samples in ARUPS. Thus, one needs to use oriented thin films on conductive substrates to realize the measurement. Organic thin films, being free from charging, are divided into two groups: (i) uniaxially oriented thin films where direction of the periodic structure or molecular stacking direction is along the surface normal, and (ii) oriented thin films where direction of the periodic structure (one-dimensional molecules) or molecular stacking direction is along the surface. For the former, in order to tune $k_{\perp}$ and probe the electronic band existing along the periodic direction perpendicular to the substrate, experimental setup is chosen such that the electrons are collected normal to the surface ($\theta = 0°$), that is, $k_{//}$ is

zero, while varying $h\nu$ of the incident photons (method II). The latter is similar to the measurements of the single crystal with method I.

The use of actual single crystal in UPS measurements requires elimination of the charging effects by using high-quality single crystal with less charge-trapping centers as well as using photoinduced-electron injection from the substrate to the crystal to reduce the number of the trapped holes. An example of the dispersion measurements of single crystals will be discussed in 3.3.2.

3.3.2
Energy Band Dispersion and Band Transport Mobility

If the intermolecular band dispersion [$E_B = E_B(k)$] is measured with angle-resolved UPS (ARUPS), the effective mass of hole (m_h^*) is obtained experimentally as [28]

$$m_h^* = \hbar^2 \left[\frac{d^2 E_B(k)}{dk^2} \right]^{-1} \tag{3.11}$$

In the case that the band dispersion is described by a tight binding model, $E_B(k) = E_0 - 2t\cos(ak)$, m_h^* becomes

$$m_h^* = \hbar^2 \left[\frac{d^2 E_B(k)}{dk^2} \right]^{-1} = \frac{\hbar^2}{2ta^2} \tag{3.12}$$

where E_0 is the energy of the band center, t is the transfer integral that specifies the intermolecular interaction, and a is the lattice constant for relevant direction. Here, for the tight binding dispersion, the cosine curve is approximated by a parabola near the top of the band. In a broadband model (bandwidth (W) $> k_B T$), the drift mobility of a hole (μ_h) can be estimated from the uncertainty principle [27]:

$$\tau \geq \frac{\hbar}{W}, \quad \tau \geq \frac{\hbar}{k_B T} \tag{3.13}$$

$$\mu_h = \frac{e\tau}{m_h^*} \geq \frac{e\hbar}{m_h^* W} \cong 20 \frac{m_0}{m_h^*} \cdot \frac{300}{T} \tag{3.14}$$

where τ is the relaxation time of the hole due to scattering and T is the temperature.

The first experimental determination of intermolecular band dispersion was reported by Hasegawa *et al.* [42] for an oriented thin film of bis(1,2,5-thiadiazolo *p*-quinobis(1,3-dithiole) (BTQBT). They used an oriented multilayer (30 Å) grown on a cleaved MoS_2 single-crystal surface with the molecular planes nearly parallel to the surface, as confirmed by the quantitative analysis of the photoelectron angular distribution [43]. The $h\nu$ dependence of the normal-emission ARUPS in the HOMO and HOMO-1 region is shown in Figure 3.5a, where the periodic binding energy shifts are seen for both the HOMO and the HOMO-1 bands. The band dispersions obtained from these results are shown in Figure 3.5b, where V_0 was used as an adjustable parameter to obtain the expected periodicity in the extended Brillouin zone scheme from the tight binding model. Although the accuracy of the determined k values depends also on the number of the repeating units, the experimental dispersion relation shows a cosine curve, suggesting both bands can be

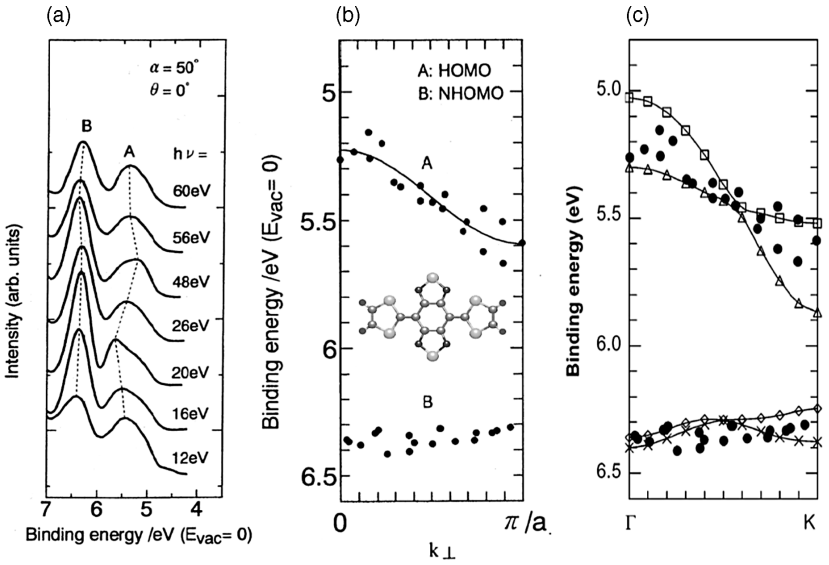

Figure 3.5 $h\nu$ dependence of ARUPS at normal emission for BTQBT thin film on MoS_2 (a) [43]. The HOMO and HOMO-1 bands are labeled A and B, respectively. HOMO and HOMO-1 band dispersion of BTQBT measured with ARUPS with a best-fit tight binding dispersion (b) [43]. Comparison with recent theoretical HOMO (□, △) and HOMO-1 (◇, ×)-derived band structure along Γ–K compared with ARUPS-derived results (•) (c) [45]. The binding energy of the theoretical bands was obtained by setting the HOMO-1-derived bands to have the same binding energy as the experimental value at Γ point. Figures a and b were reprinted with permission from Ref. [43]. Copyright (1993) by the American Physical Society, and Figure c were reprinted with permission from Ref. [45]. Copyright (2005) American Chemical Society.

approximated by the tight binding model. The experimental bandwidth W is about 0.4 eV for the HOMO band and 0.1 eV for the HOMO-1 band. Since W is given by $4t$ in the tight binding model in one dimension, the cosine curve fitting with t, $a_\perp$ (lattice spacing), and V_0 as adjustable parameters yielded $t_{\mathrm{HOMO}} = 0.092$ eV and $t_{\mathrm{HOMO\text{-}1}} = 0.02$ eV, with $a_\perp = 3.4$ Å and $V_0 = -12.5$ eV, respectively. This lattice spacing corresponds well to that (3.45 Å) of the molecular sheets in the reported crystal structure [44]. The hole mobility is then estimated as $\mu_h \geq 6.5\,\mathrm{cm}^2/(\mathrm{V\,s})$ at 290 K. Huang and Kertesz computed the band structure of BTQBT using first-principle density functional theory (DFT) and compared with the experimental dispersion [45]. The results are shown in Figure 3.5c, indicating that the data scattering in the experimental results came from two bands of the HOMO.

In Figures 3.6 and 3.7, the results of PTCDA on MoS_2 [35] and pentacene on Cu(110) [46] are shown, respectively. For pentacene (Pn), the values of m_h^* in the Γ–X_{Pn} and Γ–Y_{Pn} directions at 300 K are $3.02m_0$ and $1.86m_0$, respectively. This result also demonstrates the presence of the anisotropy of the hole mobility in pentacene crystals at higher temperatures. Furthermore, by comparing with the other experimental $E(k)$ relations in pentacene films [47–49], it was confirmed that the band structure of pentacene films is very sensitive to the minor difference in the film structure, especially molecular tilt angle, because of bumpy spatial-distribution

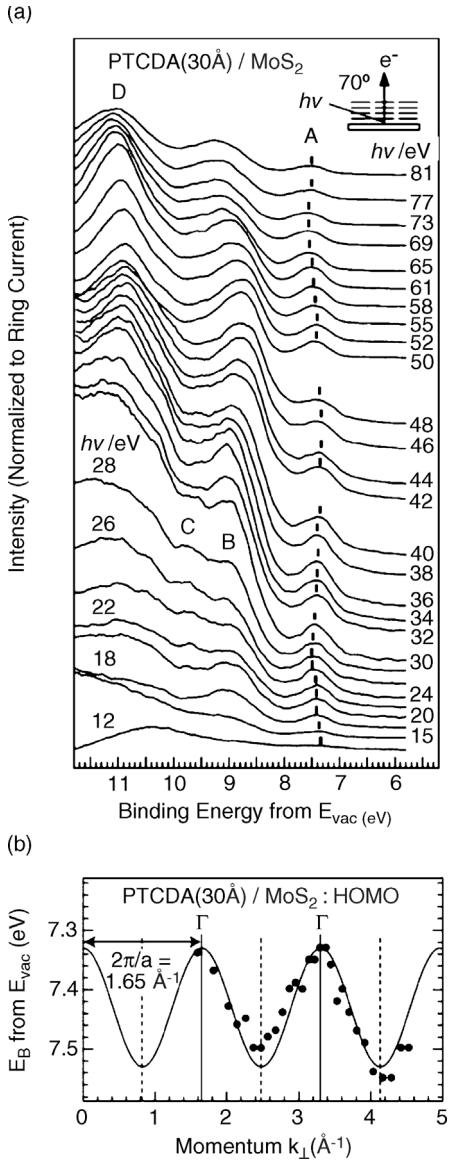

Figure 3.6 $h\nu$ dependence of ARUPS spectra along the surface normal for the 30 Å thick PTCDA multilayer (~8 ML) prepared on the MoS_2 surface (a) and the HOMO band dispersion (b) [35]. The binding energy (E_B) scale refers to the vacuum level (E_{vac}). The energy of the band center, the transfer integral, the lattice spacing normal to the surface, and the inner potential are $E_0 = 7.43$ eV, $t = 0.05$ eV, $a_\perp = 3.8$ Å, and $V_0 = -5.1$ eV, respectively. Figures were reprinted with permission from Ref. [35]. Copyright (2003) by the American Physical Society.

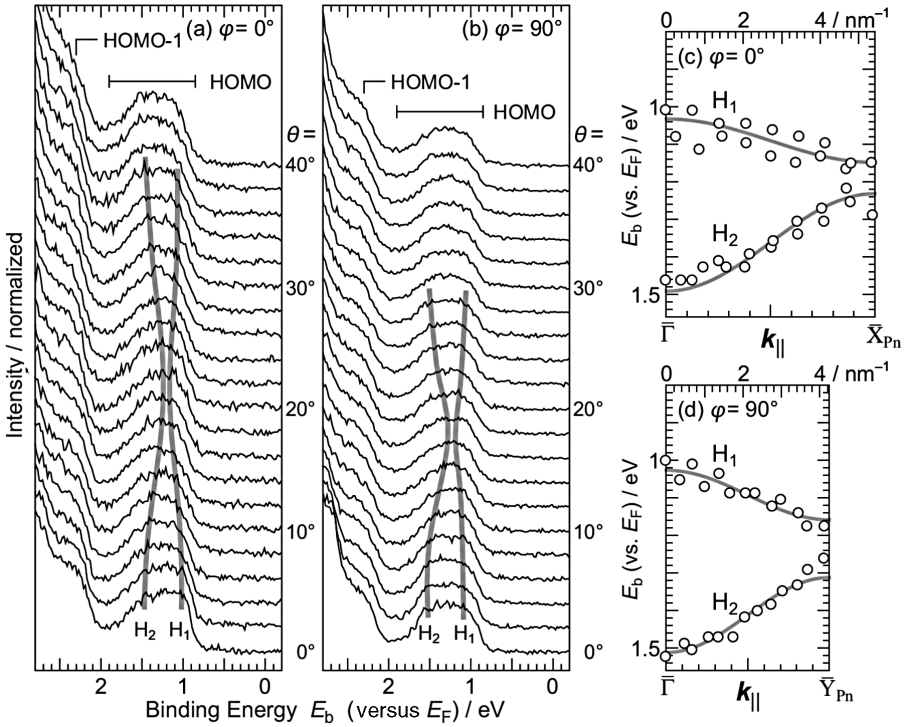

Figure 3.7 Photoelectron takeoff angle (θ) dependence of the ARUPS spectra for the highly ordered upright standing pentacene multilayer film on Cu(110) measured at (a) $\phi = 0°$ and (b) $\phi = 90°$ and the experimental HOMO band dispersion [46]. The incidence photon energy is 20 eV and the sample temperature is 300 K. E_b is the binding energy relative to the Fermi level (E_F) of the substrate. (c and d) $E(k_{||})$ relation for the highly ordered upright standing pentacene multilayer film on Cu(110) at sample azimuthal angle (c) $\phi = 0°$ and (d) $\phi = 90°$. ϕ is measured from [110] direction. Figures were reprinted with permission from Ref. [46]. Copyright (2008) Wiley.

of MO of the molecule. This was also shown with band structure calculation [50]. Further studies on the correlation between the band structure and the film structure would lead to a breakthrough for the understanding of the charge transport mechanism in organic solids.

So far some other dispersion measurements are available for oriented thin films [28]. These measurements used oriented thin films to avoid charging effects upon photoionization.

Recently, band dispersion measurement of a single crystal was realized by Machida *et al.* for rubrene that showed the largest mobility so far [51]. The results are shown in Figure 3.8. The HOMO band dispersion width was found to be 0.4 eV along the Γ–Y direction (well-stacked *b*-direction), whereas it is very small along the Γ–X direction (*a*-direction). The dispersion along the Γ–Y direction gives $m_h^* = 0.65(\pm 0.1)m_0$ using Eq. (3.12). In the case of rubrene single crystal, if the reliable μ_h is known, we can also obtain τ or mean free path (l_h)

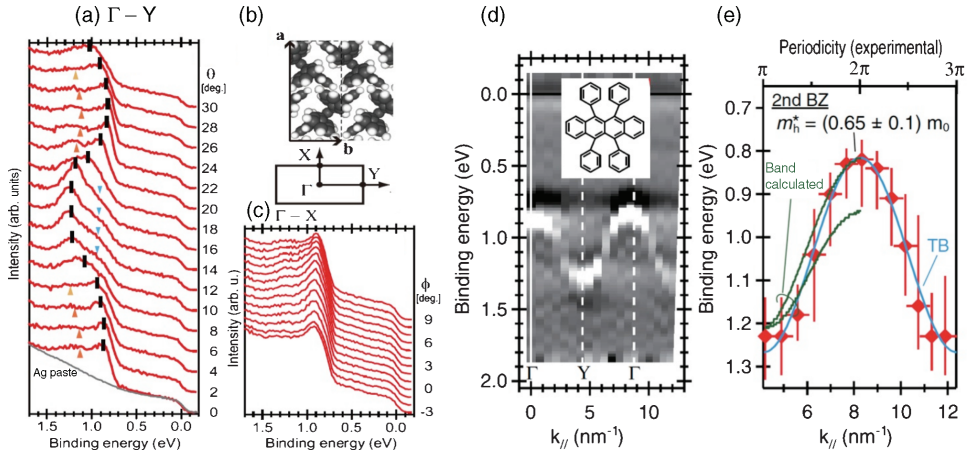

Figure 3.8 ARUPS spectra of a rubrene single crystal and band dispersion [51]. (a) The spectra along the Γ–Y direction (*b*-direction of the crystal). The upward and downward triangles indicate the high and low E_B shoulders, respectively. The bottom curve represents a spectrum of the silver paste. (b) Schematics of molecular orientation of the crystalline *a*–*b* plane ($a = 1.44$ nm, $b = 0.72$ nm) [52] and the corresponding reciprocal lattice. (c) ARUPS spectra along the Γ–X direction. The main peak position at each θ is marked with a thick bar. (d) Second derivative of the ARUPS spectra mapped on the E–$k_{//}$ plane. Center and boundary of the Brillouin zone are also indicated by dashed lines. (e) E–$k_{//}$ diagram of the main peaks along the Γ–Y direction in the second BZ. Theoretical band dispersions [53] and a fitting curve obtained by the tight binding approximation (TB) are also shown. Figures were reprinted with permission from Ref. [51]. Copyright (2010) by the American Physical Society.

of the HOMO hole by combining experimental m_h^* and μ_h to be $\tau = 15$ fs and $l_h = 2.1$ nm or longer. This distance is three times larger than the lattice constant, suggesting that the transport behavior in the HOMO band of the rubrene single crystal may be described by coherent band transport. Similar results were obtained by Ding *et al.* [54].

3.3.3
Density-of-States Effects in Polycrystalline Film

The HOMO band dispersion in pentacene suggests that there is a density-of-states (DOS) structure and, therefore, the DOS may be observed even for polycrystalline films. Such evidences were observed by Fukagawa *et al.* [55] prior to the band dispersion measurements and accelerated the ARUPS experiments. The DOS structure in the HOMO band of polycrystalline pentacene is shown in Figure 3.9. Actually the maximum difference in binding energy between the higher E_B band and the lower E_B one in Figure 3.9, 460–500 meV, is in good agreement with the largest energy separation between two components of the HOMO (Figure 3.7) [46, 49]. The two DOS components of polycrystalline pentacene were better resolved even for polycrystalline monolayer when it is prepared

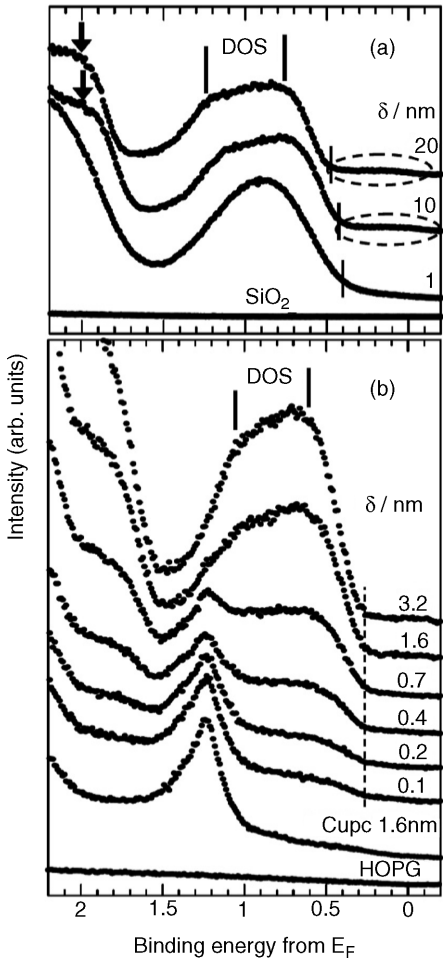

Figure 3.9 He I UPS spectra of pentacene/SiO_2/Si(100) (a) and pentacene/CuPc/HOPG (b) as a function of the deposition amount of pentacene (δ) in the HOMO region [55]. In part (b), the underlying CuPc film consists of flat-lying CuPc. All the spectra were measured at 295 K. Bars indicate density-of-states (DOS) structure of the pentacene HOMO band. Figures were reprinted with permission from Ref. [55]. Copyright (2006) by the American Physical Society.

on CuPc(ML)/GeS(001) and CuPc(ML)/HOPG [56], where the surfaces of GeS(001) and HOPG are passivated by flat-lying CuPc(ML). Note that one can obtain a clear evidence of the intermolecular band dispersion even for the poly-crystalline film of monolayer range when the molecular packing structure in each grain is sufficiently good. If such DOS splitting is not observed, one should understand that the molecular packing in the film is not sufficient, thus yielding a very low μ_h in pentacene field-effect transistor (organic field-effect transistor OFET).

3.4
Electron–Phonon Coupling, Hopping Mobility, and Polaron Binding Energy

3.4.1
Basic Background

Traveling charges couple strongly with phonons, and the hopping charge mobility is dominated by the so-called electron–phonon coupling. Here, phonons involve both delocalized lattice phonons and localized phonons at each molecule in a molecular solid. The latter corresponds well to molecular vibrations of a free molecule; thus, in many cases, we use electron–vibration coupling as the keyword when we consider the coupling with localized phonons. For hole transport, it is necessary to consider hole–vibration coupling, which in principle can be measured by UPS as vibration-related shake-up satellites of a spectral peak (HOMO for hole conduction in organic devices).

Direct experimental evidence of HOMO hole–vibration coupling in organic semiconductor film was published in 2002 [33]. A HOMO band in UPS involves information on the coupling between the conduction hole and vibrations of the molecular ion. UPS measurements can thus offer key information that is necessary to unravel the fundamental mechanism in the carrier transport properties of organic devices.

Charge hopping dominates the mobility of molecular systems with very narrow bandwidths and systems with larger bandwidths if the mean free path of the conduction charge is on the order of the intermolecular distance. Charge transfer processes and carrier dynamics of organic molecules have been widely studied in various fields and detailed theoretical descriptions can be found in several reviews [29–32, 57]. According to general microscopic models, total mobility can be expressed as the sum of two contributions, that is, (i) coherent charge tunneling that dominates transport at low temperatures, and (ii) incoherent charge hopping that becomes dominant at high temperatures. The relative contributions of either mechanism depend on the film structures, where key parameters are the charge (electron or hole)–phonon (molecular vibration) coupling, the electronic bandwidth, and phonon bandwidths. For ideal crystalline films, the model has been satisfactorily described in the theoretical work for two limiting cases, that is, weak and strong electronic coupling limits; however, a model that exhibits intermediate coupling with dependence on temperature has not yet been well explained.

The Holstein polaron model [58, 59] has been applied within the limits of weak intermolecular interactions. There is also a detailed theoretical description in a review [31, 32]. Since the electronic state concerned is well localized, charge transport occurs via hopping from one molecule to the next. Transport in a wide band is also described by hopping when the mean free path of the mobile charge is very short [28]. Moreover, changes in the hopping rate due to variation of relative intermolecular geometry need to be considered for static disorder systems, which are often found in actual organic solids. When an electron or a hole is injected into a

molecular solid, electronic–nuclear coupling leads to localization and transport occurs via localized charge hopping, which is closely related to Marcus electron transfer theory [29]. The semiclassical Marcus hopping model for self-exchange charge transfer has been widely studied. Here, we present one semiclassical approach to obtain hopping mobility. These molecular parameters have appeared in the following equations, which have also often been used in other theoretical models and can experimentally be obtained by using high-resolution UPS measurements.

The hopping mobility (μ) in the high-temperature regime can be approximated from the electron transfer rates by considering the Einstein relation for diffusive motion [28, 31]:

$$\mu = \frac{ea^2}{k_B T} k_{CT} \quad \text{and} \quad k_{CT} = \frac{2\pi}{\hbar} t^2 \sqrt{\frac{1}{4\pi\lambda k_B T}} \exp\left[-\frac{\lambda}{4k_B T}\right] \tag{3.15}$$

where a is the intermolecular distance, k_{CT} is the charge transfer/hopping probability per unit time, λ denotes the reorganization energy induced by the charge transfer, and t corresponds to the intermolecular transfer integral that describes the strength of the electronic interaction between adjacent molecules, as in Eq. (3.12). Thus, there are two major parameters that determine the charge hopping mobility: (i) the electronic coupling (transfer integral t) between adjacent molecules, which needs to be large, and (ii) the reorganization energy λ, which needs to be small for obtaining efficient hopping mobility. For the hole, transport t can be experimentally obtained from the HOMO band dispersion of a molecular stacking system or from the splitting of the HOMO level of a dimer molecule. λ corresponds to the sum of the geometry relaxation energies ($\lambda_{rel}^{(1)}$ and $\lambda_{rel}^{(2)}$) in Figure 3.10. The contribution of each vibration mode to relaxation energy $\lambda_{rel}^{(2)}$ can be determined by the intensities of vibration satellites in high-resolution UPS. The satellite intensities

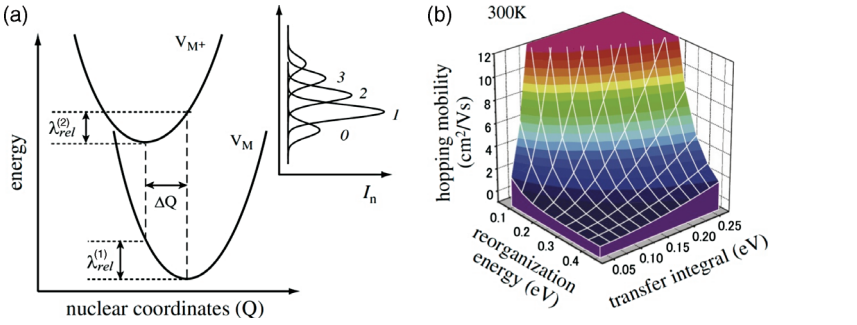

Figure 3.10 (a) Typical adiabatic energy surfaces of neutral (V_M) and ionized (V_{M+}) states and two relaxation energies $\lambda_{rel}^{(1)}$ and $\lambda_{rel}^{(2)}$ at ionization ($M \rightarrow M^+$) and neutralization ($M^+ \rightarrow M$) processes. The UPS intensity of vibration satellites I_n on photoionization is shown on the right. $\lambda_{rel}^{(2)}$ is obtained by measuring I_n. (b) Typical simulation results of charge hopping mobility as function of transfer integral (t) and reorganization energy ($\lambda = 2\lambda_{rel}^{(2)}$ using Eq. (3.15) at 300 K and $a = 0.32$ nm. Figures were reprinted with permission from Ref. [34]. Copyright (2009) Elsevier.

are described by the values of the Huang–Rhys factors S, which in the harmonic approximation are related to $\lambda_{\mathrm{rel}}^{(2)}$ by

$$\lambda_{\mathrm{rel}}^{(2)} = \sum_i S_i h\nu_i \tag{3.16}$$

There are two λ_{rel} components $\lambda_{\mathrm{rel}}^{(1)}$ and $\lambda_{\mathrm{rel}}^{(1)}$, corresponding to going to the ionized state and returning to the neutral state (Figure 3.10). If $\lambda_{\mathrm{rel}}^{(1)}$ is not too different from $\lambda_{\mathrm{rel}}^{(2)}$, λ can be written as

$$\lambda = \lambda_{\mathrm{rel}}^{(1)} + \lambda_{\mathrm{rel}}^{(2)} \approx 2\lambda_{\mathrm{rel}}^{(2)} \tag{3.17}$$

One thus obtains λ using the following relation:

$$\lambda \approx 2\lambda_{\mathrm{rel}}^{(2)} = 2\sum_i S_i h\nu_i \tag{3.18}$$

When the neutral state is in the vibrational ground state, the intensities of the vibrational progression resemble a Poisson distribution:

$$I_n = \frac{S^n}{n!} e^{-S} \tag{3.19}$$

where I_n is the intensity of the nth vibrational satellite. These relations mean that λ can be experimentally estimated by measuring $h\nu_i$ and I_n with high-resolution UPS. As Eq. (3.15) is too simplified when we calculate μ using experimental λ obtained at low temperatures, one should refer, for example, to Refs. [31, 32]. To our knowledge, however, no good theoretical description is available so far to obtain μ or k_{CT} from the analyses of the vibration satellites in the thin-film UPS measured at low temperatures.

Here, one should be careful in considering the hopping mobility obtained by above-described approach, since (i) the validity of the Einstein relationship has been debated for nonequilibrium conditions, for example, in an actual organic field-effect transistor, and (ii) the above-described hopping mobility corresponds to that in an ideal crystalline region, where there is no energy distribution/-spread of the HOMO. For nonideal crystals, which have various band gap states/trap states due to crystal imperfectness and domain boundaries, we need to consider distributions of the electronic energy levels, the intermolecular distance that depends on relative molecular orientation of relevant adjacent molecules and t, and thus the progress of theoretical study on these contributions as well as on the effects of polaron, as discussed in Section 3.2.2 [32, 57]. It is true, however, that μ in actual devices of poor molecular packing should be smaller than that estimated with above-described method.

As the polaron binding energy (E_{pol}) is defined as a stabilization energy when the hole (electron) is localized on a single lattice site, E_{pol} is directly related to the relaxation energy and thus the reorganization energy [32]. For intramolecular relaxation (for a very small positive polaron) in the limit of weak intermolecular electronic

interaction ($t \sim 0$), E_{pol} may be obtained by using $\lambda_{rel}^{(2)}$ determined from the UPS vibration satellites:

$$E_{pol} = \lambda_{rel}^{(2)} \cong \frac{\lambda}{2} \tag{3.20}$$

This relation means that the high-resolution UPS gives E_{pol} even for molecular systems with $\lambda_{rel}^{(1)} \neq \lambda_{rel}^{(2)}$.

3.4.2
Experimental Reorganization Energy and Polaron Binding Energy

The bandwidth of UPS features contains information on electron/hole–phonon/vibration interaction, electron (hole) lifetime, and electron-defect scattering provided that the final state band structure (dispersion) effects are not taken into account. It is necessary to obtain high-resolution UPS spectra to observe vibration satellites for HOMO band. There are few examples of molecular adsorbates on metal surfaces where vibrational features can be resolved in a valence photoemission spectrum and where structural heterogeneity can be eliminated from molecule–metal interfaces to allow the bandwidth to be quantitatively determined.

The first result for a CuPc submonolayer (ML) on HOPG [33] is shown in Figure 3.11, where the molecular plane is parallel to the surface. This result was

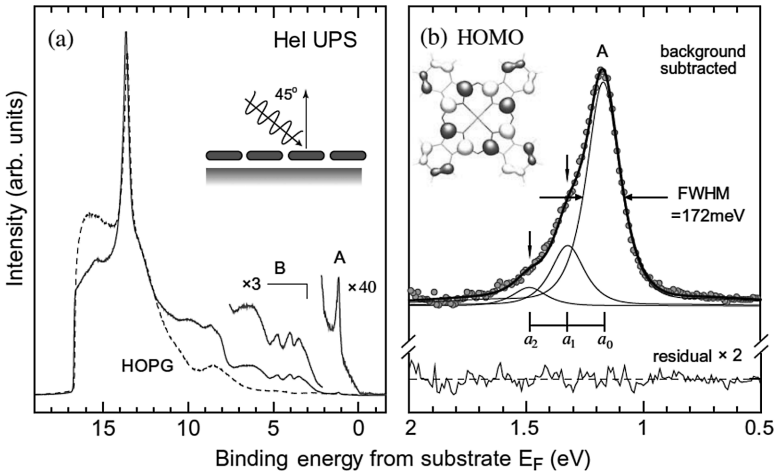

Figure 3.11 (a) He I UPS of CuPc (0.2 nm) on a highly oriented pyrolytic graphite (HOPG) substrate (solid curve) and clean HOPG (dashed curve) at the sample temperature of 295 K at $\theta = 0^\circ$ [33]. (b) Expanded spectrum of top band (A) (HOMO) region after subtraction of background. Circles represent observed spectrum after subtraction of background. Three components (a_0–a_2) of pseudo-Voigt profiles used in curve fitting are indicated by thin solid curves. Solid curve that overlaps observed spectrum is convolution of three fitting curves. Residual of curve fitting is also shown at bottom of (b). Orbital pattern of HOMO of CuPc is also illustrated. Caution should be taken with vibration energy (170 meV) obtained from this result. More precise measurements give smaller vibration energy (153 meV) as shown in Figure 3.12 Figures were reprinted with permission from Ref. [33]. Copyright (2002) Elsevier.

obtained at room temperature (295 K), since the molecular orientation becomes tilted to yield a larger spectral bandwidth at a lower temperature due to the appearance of a nonuniform packing structure [60]. Nevertheless, the experiment was successfully realized in obtaining a much sharper HOMO band for the CuPc/HOPG system, which will be discussed later, by properly controlling the method of cooling. The HOMO (labeled A) in Figure 3.11a appears as a sharp peak at 1 eV below E_F. Panel (b) shows an enlarged view of the HOMO peak after the contribution from the HOPG substrate has been subtracted. The peak is asymmetric and can be decomposed into three vibrational features ($\nu = 0, 1, 2$) with an energy separation of 170 meV (this value has been improved in recent work) (Figure 3.12). This gives a full width at half maximum (FWHM) of 172 meV for the main component ($\nu = 0$). Considering an instrument resolution (ΔE) of 80 meV, the intrinsic linewidth was obtained as 150 meV, which corresponds to a lifetime of 2.2 fs under the

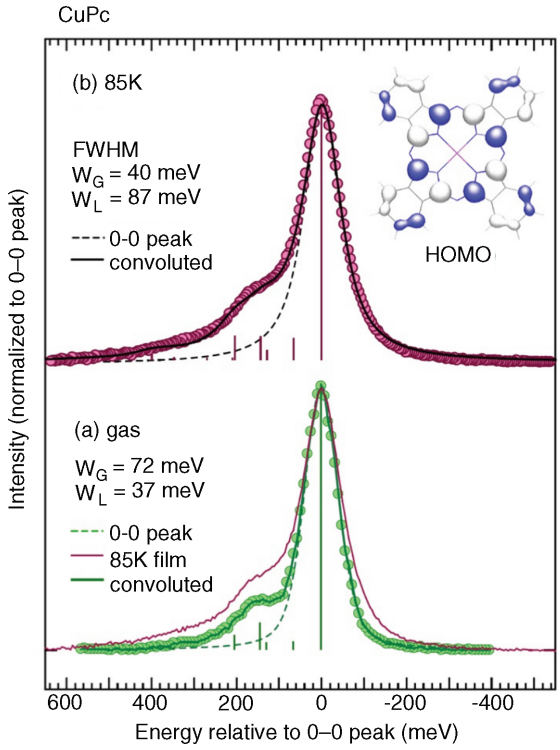

Figure 3.12 Gaseous (green circles) and angle-integrated-ML UPS spectra (red circles) for CuPc, compared with convoluted curves of eight vibrational modes (solid curves) [34]. Energy is relative to 0–0 transition peak (dashed curve). (a) Convolution curve obtained by Voigt functions ($W_G = 72$ meV, $W_L = 37$ meV) with S_{gas} and $h\nu_{gas}$, compared with gas-phase and 85 K film spectra (thin curve). Vertical bars indicate 0–0, 0–1, and 0–2 transition intensities. (b) Convolution curve obtained by Voigt functions ($W_G = 40$ meV and $W_L = 87$ meV) with S_{film} and $h\nu_{gas}$. Each S_{film} in this analysis was determined by least-squares fitting. Gas spectrum is after Evangelista *et al.* [66]. Figure was reprinted with permission from Ref. [34]. Copyright (2009) Elsevier.

assumption of using an uncertainty relation. The lifetime effect on the line shape will be discussed elsewhere without using the uncertainty relation. This value can be an upper limit for the lifetime of the hole generated by the photoemission process. The transient hole was considered to be filled by electron transfer from the HOPG substrate; thus, the lifetime of the HOMO hole may correspond to the electron transfer rate to the HOMO.

Figure 3.13 shows the angle-integrated UPS spectra ($\theta = 0°$–$60°$) of a pentacene (ML)/HOPG system compared with the convoluted curves of 18 A_g modes [61]. The energy scale is relative to the 0–0 transition peak. Here, the thin-film spectra have also been integrated for the azimuthal angle around the surface normal by the azimuthal disorder of the single-crystal domains in the HOPG surface. The convolutions were carried out using Voigt functions, in which the

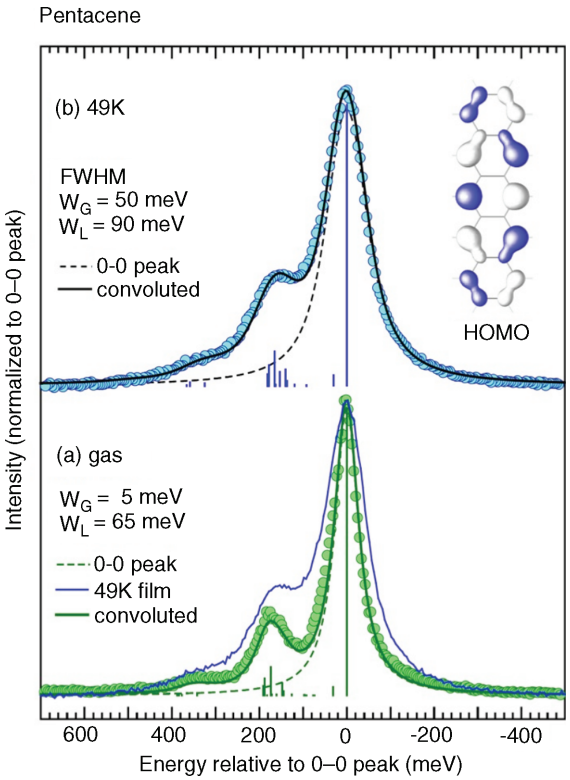

Figure 3.13 Gaseous (green circles) and angle-integrated ML UPS spectra (blue circles) for pentacene compared with convoluted curves of 18 A_g vibrational modes (solid curves) [34, 61]. Energy is relative to 0–0 transition peak (dashed curve). (a) Convolution curve obtained by Voigt functions ($W_G = 5$ meV and $W_L = 65$ meV) with S_{gas} and $h\nu_{gas}$, compared with gas-phase and 49 K film spectra (thin curve). Vertical bars indicate 0–0, 0–1, and 0–2 transition intensities. (b) Convolution curve obtained by Voigt functions ($W_G = 50$ meV and $W_L = 90$ meV), assuming values of 1.2 S_{gas} and 0.95 $h\nu_{gas}$. Gas spectrum is after Malagoli *et al.* [62]. Figure was reprinted with permission from Ref. [34]. Copyright (2009) Elsevier.

intensity of the vibration satellite is given by 0–0, 0–1, and 0–2 transitions as represented by the Poisson distribution. The convoluted curve with $W_G = 5$ meV and $W_L = 65$ meV for Voigt functions and with the vibration intensities given by the gas-phase S factor (S_{gas}) and the gas-phase vibration energies (h_{ngas}), which were used to analyze the gas-phase spectrum [62], is in excellent agreement with the gas-phase spectrum to yield a λ_{gas} of 97 meV. However, there was marked disagreement between this convoluted curve and the 49 K spectrum both in the satellite intensities and the linewidth. Better agreement between the 49 K and the convoluted spectrum is obtained for $W_G = 50$ meV, $W_L = 90$ meV, and $S_{film} = 1.2S_{gas}$ for all A_g vibrational modes, in which all $h\nu_{gas}$'s are contracted by 0.95, which is obtained from direct measurements of the vibration energy for the satellite peak (158 meV for 49 K film and 167 meV for gas-phase UPS). Therefore, λ for the pentacene/HOPG (λ_{film}) was obtained from Eq. (3.18) as $\lambda_{film} = 109$ meV at 49 K. The value was slightly revised to $\lambda_{film} = 110$ meV (Kera, S. and Ueno, N. *et al.*, unpublished). λ_{film} is larger than λ_{gas} [62, 63], indicating that the hole mobility at the interface and in the bulk of oligoacene crystal is smaller than that expected from the gas-phase results.

Paramonov *et al.* [64] calculated on the hole–vibration coupling on the pentacene/graphite system and demonstrated that the effects of molecule/substrate interaction on hole–vibration coupling are larger than those of intermolecular interaction. Using Eq. (3.15), the hopping mobility in a crystalline pentacene can be estimated as 1–2 cm^2/Vs from $\lambda_{film} = 0.10$–0.11 eV obtained from monolayer film, $t = 0.04$–0.06 eV from band dispersion measurements [46, 49], $a = 0.32$ nm, and $T = 300$ K. Note that λ_{film} and t depend on the direction of hopping in the crystal. In passing, Nan *et al.* reported that the semiclassical Marcus theory is valid only for very small λ and at very high temperatures by considering electronic coupling [65].

Figure 3.12 plots new angle-integrated UPS spectra ($\theta = 0$–$60°$) for the CuPc (ML)/HOPG system with the gas-phase results [66] and FC analysis on the Pc system by Kera *et al.* [34, 56]. Here, sharper HOMO bands are observed for ML film than those were evident in the previous results (Figure 3.11) by measuring the UPS using the electron energy analyzer with a higher energy resolution ($\Delta E < 20$ meV) and by controlling the sample preparation more carefully. The FWHM of the 0–0 peak for the integrated spectrum is about 120 meV. The convolutions were done using Voigt functions as was described for pentacene. The convoluted curve with $W_G = 72$ meV and $W_L = 37$ meV for the Voigt functions was used for the gas-phase spectrum. The vibrational fine structure of the gas-phase CuPc was reproduced well using eight vibrational modes (A_g and B_{1u}) whose intensities satisfied the linear coupling model. We used up to eight vibration modes with the largest S factors to reduce computation costs, that is, other modes with smaller S factors were considered in a spectral width. We found that the k for the CuPc was $\lambda_{gas} = 63$ meV from the gas-phase results. This value is similar to the results recently estimated from theoretical calculations for TiOPc [67].

In Figure 3.14, we show values of the relaxation energy $\lambda_{rel}^{(2)}$, namely, $\lambda_{film} \cong 2\lambda_{rel}^{(2)}$ and polaron binding energy E_{pol} (intramolecular polaron), which have been

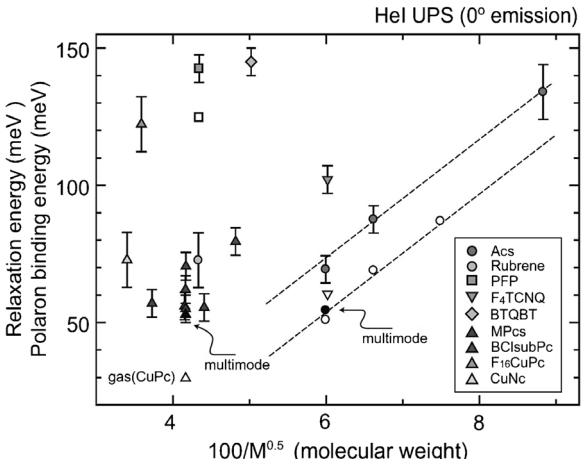

Figure 3.14 Experimental relaxation energy ($\lambda_{rel}^{(2)}$) and polaron binding energy (E_{pol}) versus $100/M^{0.5}$ (M: molecular weight) for various organic monolayer films. Reorganization energy $\lambda \cong 2\lambda_{rel}^{(2)}$ [34]. Results are for oligoacene (Ac: pentacene, tetracene#, naphthalene#), perfluoropentacene (PFP#), rubrene#, tetrafluoro-tetracyanoquinodimethane (F_4TCNQ#), bis(1,2,5-thiadiazolo)-*p*-quinobis (1,3-dithiole) (BTQBT#), metal–phthalocyanine (MPc; M = H_2, OV, OTi, ClAl, Cu, and Pb), Cu–naphthalocyanine(CuNc#), Cu–hexadecafluorophthalocyanine (F_{16}CuPc#), and chloro(subphthalocyaninato)boron (BClsubPc#). Open symbols are from gaseous results: Acs (pentacene, tetracene, and anthracene) [4], PFP#, CuPc (spectra) [66], and F_4TCNQ#, and closed symbols are for multimode analysis of pentacene and CuPc films (Figures 3.12 and 3.13). Dashed lines are visual guides. HOMO band measured at normal emission (acceptance angle of 12°) is fitted with Gaussian functions. Single normal mode (typically 150–170 meV) was considered to determine relaxation energy. Errors are estimated from residual spectra. Hash marks (#) represent that original spectra have not yet been published [34]. Figure was reprinted with permission from Ref. [34]. Copyright (2009) Elsevier.

measured so far [34], where $\lambda_{rel}^{(2)}$ and E_{pol} obtained by single-mode analysis are plotted as a function of the square root of the molecular weight (M). The relaxation energies for the films were estimated using the spectra at $\theta = 0°$ with acceptance angle of 12° and some of the solid-state effects have also been included [34]. Nevertheless, one can clearly see a correlation between the relaxation energy and the size of the π electron system for oligoacenes (Acs), as has been described in theoretical papers [31, 63]. It is interesting to see that the polaron binding energy is 0.05–0.15 eV, while the electronic polarization energy (electronic polaron binding energy) is around 1.2–1.8 eV [37].

3.5 Summary

Although many works were carried out on electrical properties of organic devices, most of them discussed *I–V* curves under classical electromagnetism with charge injection barrier estimated by UPS on organic films on polycrystalline

substrates/electrodes. In order to develop key technologies to increase device functions, it is clear that we need to understand relation between the electronic states and the electrical property.

We described what we have learnt so far, but it is more important to realize what we do not know currently. Emphasis in this chapter was therefore placed on high-precision UPS studies that can provide deeper insights into the charge mobility of organic molecular systems that have been elusive in past experimental studies on electrical conduction. The accurate information on the electronic states described here would provide a way to reach the goal of organic electronics. As impacts of imperfect molecular packing on the electronic structure are also important to unravel the energy level alignment and band bending, we will describe this issue elsewhere.

As understood from this chapter, we must know the relaxation time or mean free path of the conduction charge, namely, the mean free path of very low-energy electron and hole in an organic solid, in obtaining the drift mobility more quantitatively. Experimental challenges on this issue have been left.

Acknowledgments

The author is very grateful to the late Prof. K. Seki of Nagoya University for close collaboration for more than 30 years. He also thank Prof. S. Kera of Chiba University, Dr. H. Yamane of Institute for Molecular Science, and Dr. H. Fukagawa of NHK for their collaboration.

References

1 Akamatsu, H. and Inokuchi, H. (1950) *J. Chem. Phys.*, **18**, 810.
2 Akamatsu, H., Inokuchi, H., and Matsunaga, Y. (1954) *Nature*, **173**, 168.
3 Inokuchi, H. (2006) *Org. Electron.*, **7**, 62.
4 Ishii, H., Sugiyama, K., Ito, E., and Seki, K. (1999) *Adv. Mater.*, **11**, 605.
5 Salaneck, W.R., Seki, K., Kahn, A., and Pireaux, J.-J. (eds.) (2002) *Conjugated Polymers and Molecular Interfaces: Science and Technology for Photonic and Optoelectronic Applications*, Marcel Dekker, New York.
6 Koch, N. (2007) *ChemPhysChem.*, **8**, 1438.
7 Hwang, J., Wan, A., and Kahn, A. (2009) *Mater. Sci. Eng. R*, **64**, 1.
8 Gao, Y. (2010) *Mater. Sci. Eng. R*, **68**, 39.
9 Heimel, G., Salzmann, I., Duhm, S., and Koch, N. (2011) *Chem. Mater.*, **23**, 359.
10 Heine, V. (1965) *Phys. Rev.*, **138**, A1689.
11 Tejedor, C., Flores, F., and Louis, E. (1977) *J. Phys. C*, **10**, 2163.
12 Flores, F. and Tejedor, C. (1987) *J. Phys. C*, **20**, 145.
13 Mönch, W. (1994) *Surf. Sci.*, **299**, 928.
14 Vázquez, H., Oszwaldowski, R., Pou, P., Ortega, J., Pérez, R., Flores, F., and Kahn, A. (2004) *Europhys. Lett.*, **65**, 802.
15 Vázquez, H., Gao, W., Flores, F., and Kahn, A. (2005) *Phys. Rev. B*, **71**, 041306 (R).
16 Kahn, A., Zhao, W., Gao, W., Vázquez, H., and Flores, F. (2006) *Chem. Phys.*, **325**, 129.
17 Vázquez, H., Dappe, Y.J., Ortega, J., and Flores, F. (2007) *J. Chem. Phys.*, **126**, 144703.
18 Vázquez, H., Flores, F., and Kahn, A. (2007) *Org. Electron.*, **8**, 241.

19 Braun, S. and Salaneck, W.R. (2007) *Chem. Phys. Lett.*, **438**, 259.

20 Braun, S., Salaneck, W.R., and Fahlman, M. (2009) *Adv. Mater.*, **21**, 1.

21 Braun, S., Liu, X., Salaneck, W.R., and Fahlman, M. (2010) *Org. Electron.*, **11**, 212.

22 Ono, M., Sueyoshi, T., Zhang, Y., Kera, S., and Ueno, N. (2006) *Mol. Cryst. Liq. Cryst.*, **455**, 251.

23 Fukagawa, H., Kera, S., Kataoka, T., Hosoumi, S., Watanabe, Y., Kudo, K., and Ueno, N. (2007) *Adv. Mater.*, **19**, 665.

24 Sueyoshi, T., Fukagawa, H., Ono, M., Kera, S., and Ueno, N. (2009) *Appl. Phys. Lett.*, **95**, 183303.

25 Sueyoshi, T., Kakuta, H., Ono, M., Sakamoto, K., Kera, S., and Ueno, N. (2010) *Appl. Phys. Lett.*, **96**, 093303.

26 Mao, H.Y., Bussolotti, F., Qi, D.-C., Wang, R., Kera, S., Ueno, N., Wee, A.T. S., and Chen, W. (2011) *Org. Electron.*, **12**, 534.

27 Meier, H. (1974) Chapter 10, in *Organic Semiconductors*, vol. **2** (ed. H.F. Ebel), Verlag Chemie, Weinheim.

28 Ueno F N. and Kera, S. (2008) *Prog. Surf. Sci.*, **83**, 490.

29 Marcus, R.A. (1993) *Rev. Mod. Phys.*, **65**, 599.

30 Silinsh, E.A. and Čápek, V. (1994) *Organic Molecular Crystals: Interaction, Localization and Transport Phenomena*, Springer, Berlin.

31 Brédas, J.-L., Beljonne, D., Coropceanu, V., and Cornil, J. (2004) *Chem. Rev.*, **104**, 4971.

32 Coropceanu, V., Cornil, J., da Silva Filho, D.A., Oliver, Y., Silbey, R., and Brédas, J.-L. (2007) *Chem. Rev.*, **107**, 926 (see also Erratum, *Chem. Rev.* 2007, 107, 2165).

33 Kera, S., Yamane, H., Sakuragi, I., Okudaira, K.K., and Ueno, N. (2002) *Chem. Phys. Lett.*, **364**, 93.

34 Kera, S., Yamane, H., and Ueno, N. (2009) *Prog. Surf. Sci.*, **84**, 135.

35 Yamane, H., Kera, S., Yoshimura, D., Okudaira, K.K., Seki, K., and Ueno, N. (2003) *Phys. Rev. B*, **68**, 33102.

36 Gutmann, F. and Lyons, L.E. (1967) *Organic Semiconductors*, John Wiley & Sons, Inc., New York.

37 Seki, K. (1989) *Mol. Cryst. Liq. Cryst.*, **171**, 255.

38 Koopmans, T. (1933) *Physica*, **1**, 104.

39 Phillips, J.C. (1961) *Phys. Rev.*, **123**, 420.

40 Berglund, C.N. and Spicer, W.E. (1964) *Phys. Rev. A*, **136**, 1030.

41 Feibelman, P.J. and Eastman, D.E. (1974) *Phys. Rev. B*, **10**, 4932.

42 Hasegawa, S., Mori, T., Imaeda, K., Tanaka, S., Yamashita, Y., Inokuchi, H., Fujimoto, H., Seki, K., and Ueno, N. (1994) *J. Chem. Phys.*, **100**, 6969.

43 Hasegawa, S., Tanaka, S., Yamashita, Y., Inokuchi, H., Fujimoto, H., Kamiya, K., Seki, K., and Ueno, N. (1993) *Phys. Rev.*, **B48**, 2596.

44 Yamashita, Y., Tanaka, S., Imaeda, K., and Inokuchi, H. (1991) *Chem. Lett.*, **7**, 1213.

45 Huang, J. and Kertesz, M. (2005) *J. Phys. Chem. B*, **109**, 12891.

46 Yamane, H., Kawabe, E., Yoshimura, D., Sumii, R., Kanai, K., Ouchi, Y., Ueno, N., and Seki, K. (2008) *Phys. Status Solidi B*, **245**, 793.

47 Koch, N., Vollmer, A., Salzmann, I., Nickel, B., Weiss, H., and Rabe, J.P. (2006) *Phys. Rev. Lett.*, **96**, 156803.

48 Annese, E., Viol, C.E., Zhou, B., Fujii, J., Vobornik, I., Baldacchini, C., Betti, M.G., and Rossi, G. (2007) *Surf. Sci.*, **601**, 4242.

49 Kakuta, H., Hirahara, T., Matsuda, I., Nagao, T., Hasegawa, S., Ueno, N., and Sakamoto, K. (2007) *Phys. Rev. Lett.*, **98**, 247601.

50 Yoshida, H. and Sato, N. (2008) *Phys. Rev. B*, **77**, 235205.

51 Machida, S., Nakayama, Y., Duhm, S., Xin, Q., Funakoshi, A., Ogawa, N., Kera, S., Ueno, N., and Ishii, H. (2010) *Phys. Rev. Lett.*, **104**, 156401.

52 Chapman, B.D., Checco, A., Pindak, R., Siegrist, T., and Kloc, C. (2006) *J. Cryst. Growth*, **290**, 479.

53 Filho, D.A.d.S., Kim, E.-G., and Brédas, J.-L. (2005) *Adv. Mater.*, **17**, 1072.

54 Ding, H., Reese, C., Mäkinen, A.J., Bao, Z., and Gao, Y. (2010) *Appl. Phys. Lett.*, **196**, 222106.

55 Fukagawa, H., Yamane, H., Kataoka, T., Kera, S., Nakamura, M., Kudo, K., and Ueno, N. (2006) *Phys. Rev.*, **B73**, 245310.

56 Ueno, N., Kera, S., Sakamoto, K., and Okudaira, K.K. (2008) *Appl. Phys.*, **A92**, 495.

57 Zhu, X.-Y. (2004) *Surf. Sci. Rep.*, **56**, 1.

58 Holstein, T. (1959) *Ann. Phys.*, **8**, 325.

59 Holstein, T. (1959) *Ann. Phys.*, **8**, 343.

60 Kataoka, T., Fukagawa, H., Hosoumi, S., Nebashi, K., Sakamoto, K., and Ueno, N. (2008) *Chem. Phys. Lett.*, **451**, 43.

61 Yamane, H., Nagamatsu, S., Fukagawa, H., Kera, S., Friedlein, R., Okudaira, K.K., and Ueno, N. (2005) *Phys. Rev. B*, **72**, 153412.

62 Malagoli, M., Coropceanu, V., da Silva Filho, D.A., and Brédas, J.-L. (2004) *J. Chem. Phys.*, **120**, 7490.

63 Coropceanu, V., Malagoli, M., da Silva Filho, D.A., Gruhn, N.E., Bill, T.G., and Brédas, J.-L. (2002) *Phys. Rev. Lett.*, **89**, 275503.

64 Paramonov, P.B., Coropceanu, V., and Brédas, J.-L. (2008) *Phys. Rev. B*, **78**, 041403 (R).

65 Nan, G., Wang, L., Yang, X., Shuai, Z., and Zhao, Y. (2009) *J. Chem. Phys.*, **130**, 024704.

66 Evangelista, F., Carravetta, V., Stefani, G., Jansik, B., Alagia, M., Nazionale, L., Stranges, S., and Ruocco, A. (2007) *J. Chem. Phys.*, **126**, 124709.

67 Norton, J.E. and Brédas, J.-L. (2008) *J. Chem. Phys.*, **128**, 034701.